Outdoor Worker Stress Monitoring Electronics with Nanofabric Radiative Cooler-Based Thermal Management

Hojoong Kim, Young Jin Yoo, Joo Ho Yun, Se-Yeon Heo, Young Min Song,* and Woon-Hong Yeo*

Severe stress endangers outdoor workers who are in an exceedingly hot workplace. Although recent studies quantify stress levels on the human skin, they still rely on rigid, bulky sensor modules, causing data loss from motion artifacts and limited field-deployability for continuous health monitoring. Moreover, no prior work shows a wearable device that can endure heat exposure while showing continuous monitoring of a subject's stress under realistic working environments. Herein, a soft, field-deployable, wearable bioelectronic system is introduced for detecting outdoor workers' stress levels with negligible motion artifacts and controllable thermal management. A nanofabric radiative cooler (NFRC) and miniaturized sensors with a nanomembrane soft electronic platform are integrated to measure stable electrodermal activities and temperature in hot outdoor conditions. The NFRC exhibits outstanding cooling performance in sub-ambient air with high solar reflectivity and high thermal emissivity. The integrated wearable device with all embedded electronic components and the NFRC shows a lower temperature (41.1%) in sub-ambient air than the NFRC-less device while capturing improved operation time (18.2%). In vivo human study of the bioelectronics with agricultural activities demonstrates the device's capability for portable, continuous, real-time health monitoring of outdoor workers with field deployability.

1. Introduction

Outdoor workers exposed to hot environments or extreme heat can be at risk of heat-related illnesses (HRIs) and serious injuries. HRIs include heat stroke, exhaustion, fainting, heat cramps, and heat rash, especially exertional heat stroke, which can occur even in non-hot environments. Heat stress caused by a combination of physical activity-induced heat and environmental factors for outdoor workers can lead to unmitigated thermal strain with increased heat storage in the body, which in turn gradually increases the risk of HRIs.[1–3] The National Institute for Occupational Safety and Health estimates that up to 10 million workers in the United States are exposed to hot working conditions, including high air temperatures, radiant heat sources, and high humidity.[1] Extreme workplace stress in the United States caused over 120 000 deaths with $190 billion in public healthcare expenses per year.[4] Further, with the global warming trend expected of extreme heat waves during the next century, these stresses of outdoor populations should be managed to prevent risky HRIs and ensure safety.[5,6] Individuals with a high level

H. Kim, W.-H. Yeo
George W. Woodruff School of Mechanical Engineering
College of Engineering
Georgia Institute of Technology
Atlanta, GA 30332, USA
E-mail: whyeo@gatech.edu

H. Kim, W.-H. Yeo
IEN Center for Human-Centric Interfaces and Engineering
Institute for Electronics and Nanotechnology
Georgia Institute of Technology
Atlanta, GA 30332, USA

Y. J. Yoo, J. H. Yun, S.-Y. Heo, Y. M. Song
School of Electrical Engineering and Computer Science
Gwangju Institute of Science and Technology
Gwangju 61005, Republic of Korea
E-mail: ymsong@gist.ac.kr

Y. M. Song
Anti-Viral Research Center
Gwangju Institute of Science and Technology
Gwangju 61005, Republic of Korea

Y. M. Song
AI Graduate School
Gwangju Institute of Science and Technology
Gwangju 61005, Republic of Korea

W.-H. Yeo
Wallace H. Coulter Department of Biomedical Engineering
Georgia Institute of Technology and Emory University School of Medicine
Atlanta, GA 30332, USA

W.-H. Yeo
Parker H. Petit Institute for Bioengineering and Biosciences
Institute for Materials
Neural Engineering Center
Institute for Robotics and Intelligent Machines
Georgia Institute of Technology
Atlanta, GA 30332, USA

**ADVANCED
SCIENCE NEWS**

www.advancedsciencenews.com

**ADVANCED
HEALTHCARE
MATERIALS**

www.advhealthmat.de

of working stress are agonized by negative physical and psychological consequences, the effects on health and productivity.[7–10] Therefore, early detection and management of excessive stress are crucial to sustaining a healthy life.

Electrodermal activity, known as galvanic skin response (GSR), has received great attention due to its quantifiable measure of sympathetic arousal and cognitive status evoked by various stressors.[11–14] GSR sensors can monitor stress activities by detecting skin conductance changes from the ionic permeability of sweat gland membranes. Conventional GSR sensing systems that utilize gel-covered wet electrodes have limitations in device location, mostly in hand area, and measurement time that can interfere with long-term daily activities.[15,16] Also, rigid modules and wires can cause motion artifacts interfering with stable signal recording. Recent advances in wearable electronics have led to the development of fully integrated and scalable wireless devices for monitoring extraneous and continuous stress in everyday life.[17–19] However, recent studies still rely on rigid, bulky sensor modules affixed to the body with straps and belts tightly, which is not yet completely free from motion artifacts during daily activities. Furthermore, most stress monitoring has been conducted indoors and the effort that directly investigates physiologic stress to hard labor in hot environments is restricted to field studies.[20–22] Beyond the current wearable devices that have been successfully developed to monitor users' stress in real-time, advanced wearable devices for outdoor activities in hot environments are required to simultaneously possess excellent adhesiveness without hindrance to repetitive movements and thermal management from the external/internal heat of the device. Meanwhile, recently introduced passive radiative coolers with high solar reflectivity and thermal emissivity open up new possibilities for the thermal management of wearable devices, such as temperature control and solar energy blocking.[23–29] Essentially, passive radiative cooling is based on minimizing solar absorption and maximizing thermal radiation into outer space ($\approx$3K) through the long-wave infrared atmospheric window (i.e., 8–13 μm wavelength).[30–40] Although non-metallic cooling structures have been introduced for the cooling effects of a wearable device,[41–43] no prior study shows wireless continuous health monitoring and active thermal management with human subjects working in real-life outdoor environments.

Here, this work introduces a fully integrated wireless bioelectronic system that integrates a radiative cooler and nanomembrane sensors for reliable stress monitoring of outdoor workers in hot environments. For effective thermal management, we exploit a nanofabric radiative cooler (NFRC) material, which is composed of electrospun polyvinylidene fluoride-co-hexafluoropropylene (PVDF-HFP) as a non-metallic and flexible material. By nanofiber-induced multi-scattering, the NFRC film shows outstanding cooling performance in sub-ambient air with high solar reflectivity and high thermal emissivity. By fully covering the bioelectronics including a battery and an active wireless unit, the NFRC-integrated skin-conformal wearable device shows $\approx$41.1% lower temperature in sub-ambient air than the bare device, and the battery runtime improved by about 18.2%. For evaluation of device stability, we investigate the GSR measurements on/off skin in various weather conditions including clear and cloudy, providing potential measurement issues of device operation in a practical application. Finally, the NFRC-integrated wear-

able soft biopatch attached to an outdoor worker is demonstrated with actual agricultural activities for reliable, continuous, real-time stress monitoring, and analysis.

2. Results and Discussion

2.1. Overview of an Outdoor Worker Stress Monitoring System that Incorporates a Nanofabric Radiative Cooler for Thermal Management

Figure 1a is a conceptual overview that illustrates the physiological stress monitoring of outdoor workers (e.g., farmers) during their tasks, in which their stress is especially elevated due to the excessive heat under direct sunlight. The proposed fully integrated, soft wearable bioelectronics enables continuous, long-term monitoring of outdoor workers' stress level and wirelessly transmit the data to an external receiver to minimize interrupting their tasks during signal monitoring. Furthermore, device integration with thermal management by an NFRC allows robust device operation even under high-temperature environments caused by extreme sunlight with maintaining the device's mechanical flexibility. Figure 1b represents the schematic exploded view of the wearable device. An integrated circuit is assembled on a flexible circuit board containing a rechargeable lithium-ion polymer battery. The key functional components of integrated circuits are a microcontroller for wireless communication based on Bluetooth low energy (BLE), GSR sensing circuitry, and a thermistor for measuring skin temperature. A low-power, 24-bit analog-digital convertor (ADC, ADS1220, Texas Instruments) and a digital thermistor (TMP116, Texas Instruments) can measure GSR signal and skin temperature with 3 μV and 0.2 °C of accuracy, respectively. BLE microcontroller (nRF52832, Nordic Semiconductor) is responsible for data transmission of both temperature and GSR signals to an external device wirelessly. The detailed design and overall electrical schematics of the integrated circuit are described in Figures S1 and S2, Supporting Information. A soft silicone elastomer encloses the assembled circuit to protect the device from an outside impact and is covered with NFRC for thermal protection. The circuit and a pair of nanomembrane sensor electrodes were integrated with a breathable fabric tape processed with a silicone adhesive to affix the device onto the skin softly.

Overall, the device is low-profile (< 5 mm in thickness, 0.28 mm for the patch) and lightweight (< 9 g), and compact footprint (8.5 × 8.0 cm), providing comfortable wearability and long-term portability on the wrist skin (Figure 1c). Figure 1d shows the top view of the fully packaged soft biopatch placed on the inner wrist that can be easily and softly handled by general users. Photos in Figure 1e capture the bottom side of the device incorporating serpentine-patterned nanomembrane dry electrodes that allow the device stretchable and flexible along with the fabric substrate.[44,45] Figure 1f shows the reflectivity and emissivity of NFRC-integrated devices in comparison to those covered with a white-pigmented elastomer (WE). The NFRC has a reflectivity that is almost total in the solar spectrum, which is between 0.3–2.5 μm wavelength. This means that it stops the device from gaining energy from the sun. Additionally, the device has a high emissivity in the atmospheric window, which is between 8–13 μm wavelength, allowing it to release thermal energy into
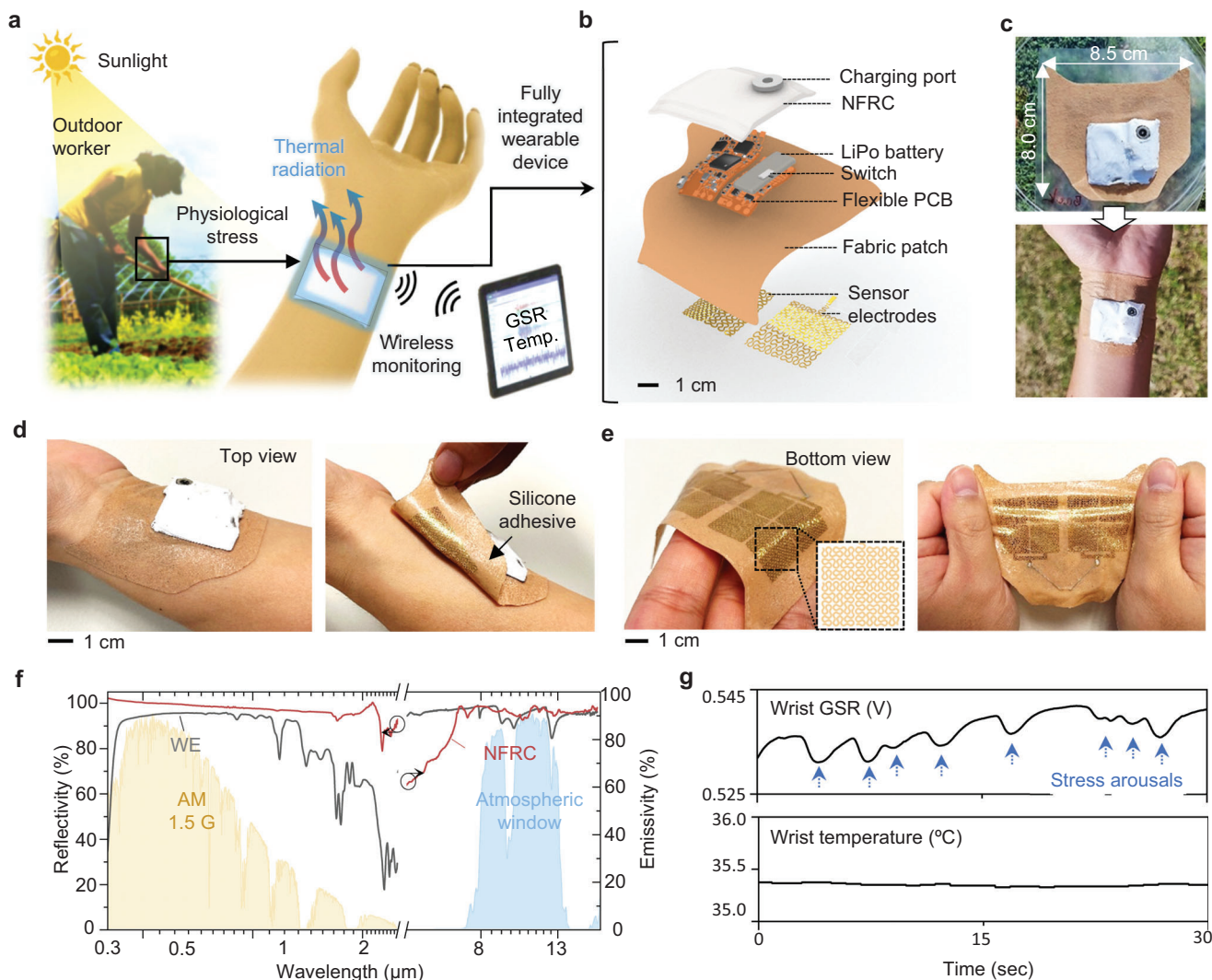
**ADVANCED
SCIENCE NEWS**

www.advancedsciencenews.com

**ADVANCED
HEALTHCARE
MATERIALS**

www.advhealthmat.de

Figure 1. Overview of a soft wearable bioelectronic system integrated with a nanofabric radiative cooler (NFRC) that enables reliable stress monitoring in an outdoor environment. a) Schematic illustration of physiological stress induced from outdoor work and wireless stress monitoring using a fully integrated wearable device with a radiative cooler. b) Schematic exploded view of the fully integrated wearable device. c) Photos of the device and that conformally attached to the inner wrist. d) Photos that capture the device placed on the wrist by simply pressing the soft membrane to the skin. e) Bottom view of the device showing serpentine-patterned electrodes enables the mechanical reliability of soft biopatch. f) Reflectivity and emissivity spectra from the visible to far-infrared wavelength range for encapsulation layers such as white elastomer (WE) and NFRC. The air mass 1.5 global (AM 1.5 G) spectrum, as a standard solar spectral irradiance distribution, was utilized. g) Raw data of galvanic skin response (GSR) and body temperature measured on the wrist. Arrows indicate the arousals when stress is induced.

outer space. Consequently, the wearable device integrated with NFRC can keep its temperature low during continuous use in hot outdoor environments that are exposed to sunlight. Successful data recording of GSR (Figure 1g, top) and skin temperature (Figure 1g, bottom) was conducted on the wrist collected with a 20 Hz of sampling rate and wirelessly transmitted to an external Android mobile device (Galaxy Tab S6 lite, Samsung) for real-time monitoring. Data packets, transmitted wirelessly, include GSR (24-bit) and temperature (16-bit) data of 50 bytes or 10 data points with a connection interval of 200 ms. The sampling rate of both parameters is 5 Hz. Signal variation of electrodermal activity triggered by physiological arousal was clearly identified in the GSR trace indicated by arrows.

2.2. Optical Characterization and Thermal Analysis of the NFRC

In this study, we fabricated a high-performance nanofabric radiative cooler as a thermal management method on the soft wearable system to provide robust device operation under high temperatures and extreme sunlight. **Figure 2**a displays photos and a scanning electron microscope (SEM) image of NFRC. After heat-pressing electrospun PVDF-HFP near the glass transition temperature for stable fabric bonding, NFRC is flexibly attached along flat glass surfaces and curved fingers (Figure 2a and details in Figure S3, Supporting Information). The NFRC is composed of fiber bundles of electrospun PVDF-HFP (Figure S4, Supporting Information), which makes them air-permeable (Figure S5,
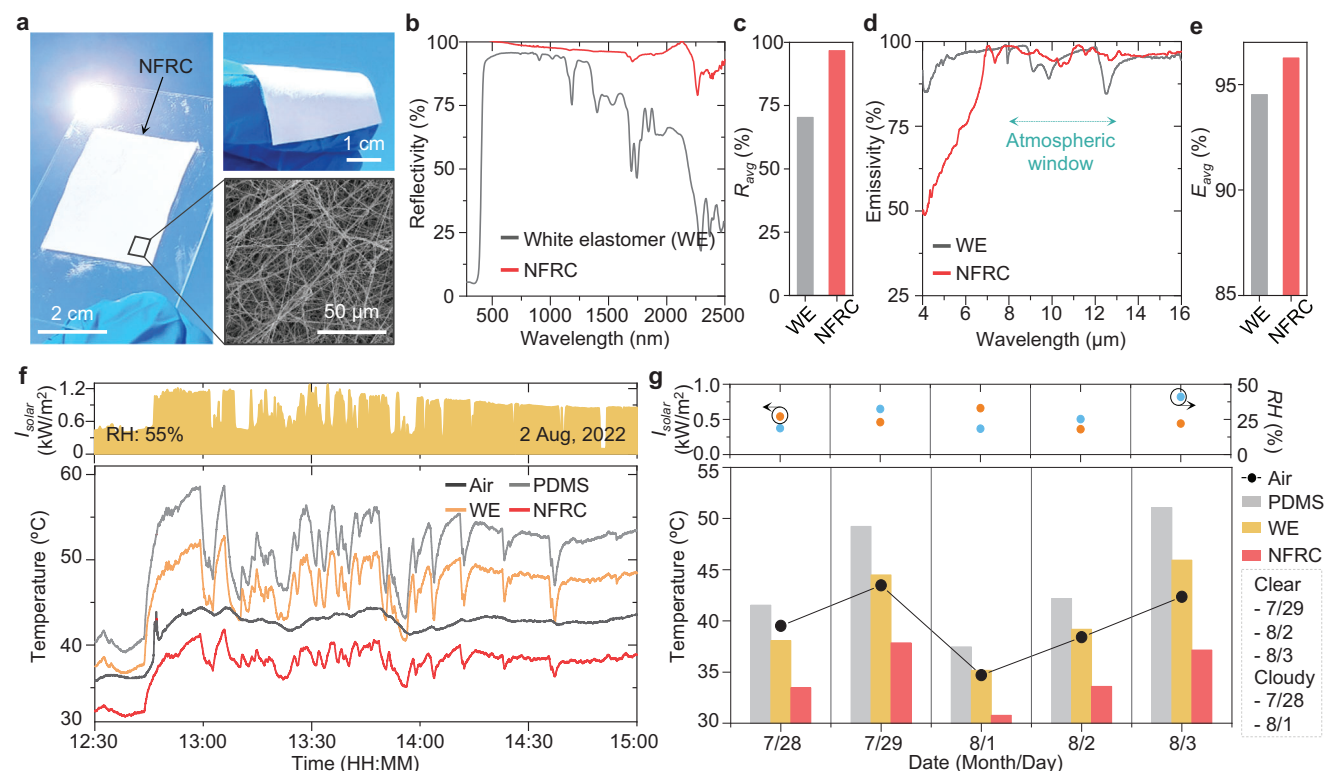
Figure 2. Optical characterization and thermal analysis of NFRC. a) NFRC on a glass slide. The top-right photo shows the device's flexibility and the bottom-right inset shows an SEM image of NFRC consisting of electrospun PVDF-HFP. b,c) Reflectivity characteristics of WE, and NFRC: b) Reflectivity spectra and c) average reflectivity at the solar spectrum. d,e) Emissivity characteristics of WE, and NFRC: d) emissivity spectra and e) average emissivity at the atmospheric window. f,g) Temperature changes at ambient air, PDMS, WE, and NFRC f) during the daytime, and g) over several days, highlighting the superior cooling effect of NFRC to air, PDMS, and WE. I_{solar} and RH indicate average solar intensity and relative humidity, respectively.

Supporting Information). The nanofibers act as effective scatterers, causing multiple Mie scattering.[46–48] This significantly improves the reflectivity of the NFRC in the solar spectrum, which ranges between 0.3–2.5 µm wavelength. Figure 2b displays the reflectivity spectra of WE and NFRC. The NFRC has a higher reflectivity than the WE in the solar spectrum, particularly in the near-infrared spectral range which spans from 1.3 to 2.5 µm wavelength. The average reflectance of NFRC is about 96%, which is 25% higher than that of WE (Figure 2c). The strong reflection of NFRCs in the near-infrared range is an additional advantage from the design point of view of the radiative cooler, since energy absorption in the near-infrared range accounts for a significant portion (11.6%) of the total solar energy. Furthermore, nanofiber structures of NFRC enhance emissivity in the atmospheric window, compared to the WE (Figure 2c). Figure 2d illustrates the emissivity spectra of WE and NFRC. The nanofiber architecture of NFRC enhances the emissivity selectively in the atmospheric window when compared to WE. Specifically, NFRC exhibits an average emissivity of 96% within the atmospheric window range, which is 2% higher than that of WE (Figure 2e). Considering its optical properties, the NFRC is anticipated to exhibit outstanding cooling capabilities through solar reflection and thermal radiation and to reduce skin/device heating, which enhances heat emission from the device (Figure S6, Supporting Information). To prove the sub-ambient cooling potential of the fabricated NFRC samples, thermocouples were affixed to the backside of

the samples to monitor temperature fluctuations. An ambient air box was also mounted to prevent the self-heating of the ambient air sensor (Figure S7, Supporting Information). Figure 2f shows the temperature measurement results of polydimethylsiloxane (PDMS), WE, and NFRC in the measurement setup. The NFRC shows sub-ambient cooling of ≈7 °C under solar power of 1051 Wm^{-2}, while PDMS and WE show higher temperatures of about 9.1 and 3.2 °C above ambient air, respectively. Further, we confirmed that NFRC has the highest cooling performance among the comparison groups regardless of the weather condition after measuring for five days (Figure 2g and details in Figure S8, Supporting Information). Overall, NFRC shows remarkable cooling performance under direct sunlight, showing suitable thermal management techniques on wearable devices for outdoor applications.

2.3. Thermal Management Analysis in the Operating State of the Wireless Wearable System

FOR THEAfter validating the cooling performance of NFRC, the effect of the thermal management technique on the basic operation performance and durability of the wireless system was identified. For thermal characterization of the device, the measurement setup was installed as shown in **Figure 3**a. To prevent heat interference from the ground, an acrylic chamber was positioned

**ADVANCED
SCIENCE NEWS**

www.advancedsciencenews.com

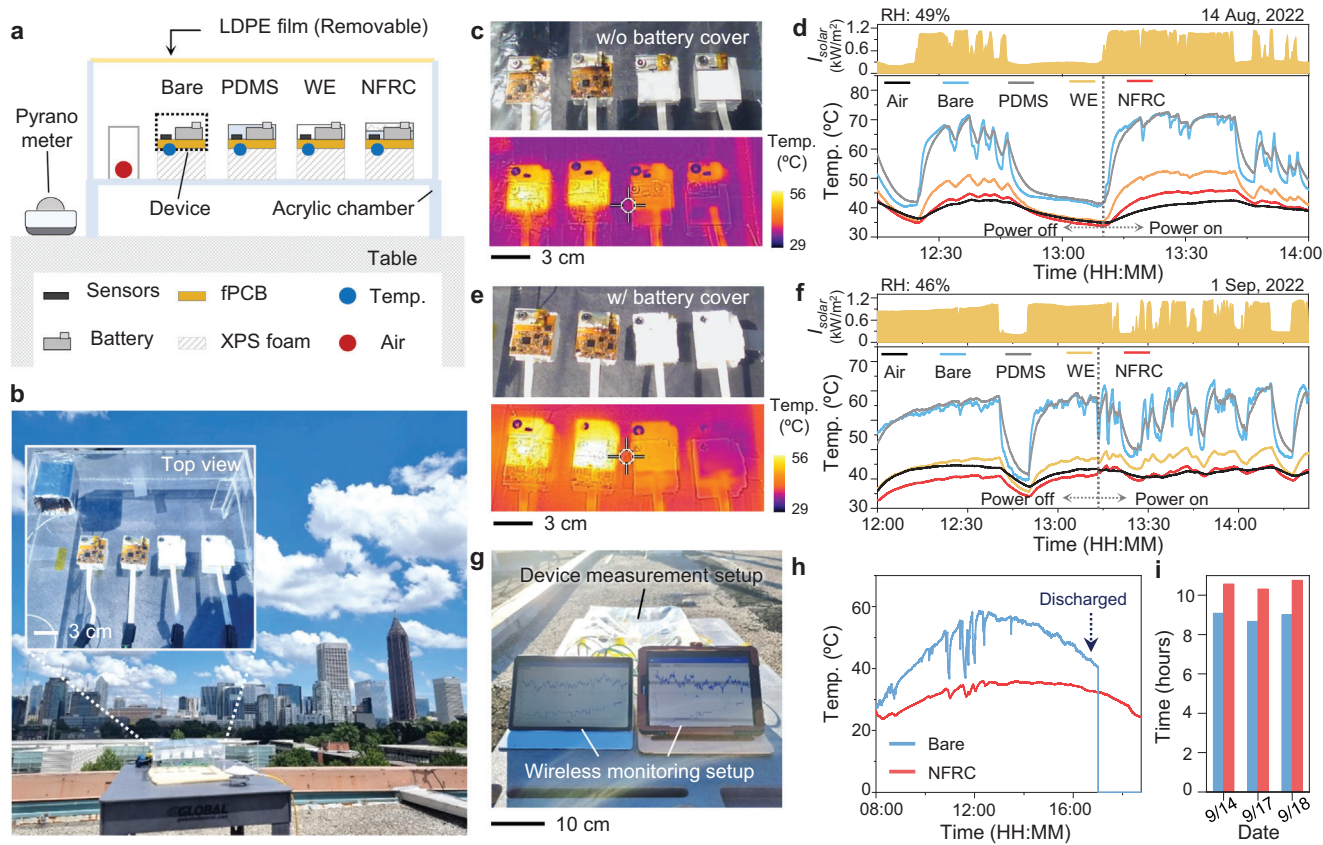**ADVANCED
HEALTHCARE
MATERIALS**

www.advhealthmat.de

Figure 3. Thermal management analysis in the operating state of a wireless system integrating with a radiative cooler. a) Schematic diagram and b) Corresponding photograph showing the setup for testing the temperature response of wearable devices with bare and with PDMS, WE, and NFRC integration in the controlled outdoor environment. c) Photograph (top) of the experimented samples (i.e., Bare, with PDMS, with WE, and with NFRC) with corresponding IR images (bottom), comparing their cooling capability on w/o battery cover. d) Temperature changes of ambient air, PDMS, WE, and NFRC without battery cover. e) Photograph (top) of the experimented samples (i.e., Bare, with PDMS, with WE, and with NFRC) with corresponding IR images (bottom), comparing their cooling capability with battery cover. f) Temperature changes of ambient air, PDMS, WE, and NFRC with battery cover. g) Photograph showing wireless monitoring of battery performance of devices with and without a radiative cooler. h) Continuous temperature monitoring to compare battery performance with and without a radiative cooler. i) Comparison of battery operation time with and without a radiative cooler.

on a table at an approximate height of 1 m. Temperature sensors were affixed to the underside of different samples, including 1) a circuit without a radiative cooler (Bare); 2) a circuit integrated with PDMS (PDMS); 3) a white elastomeric transformative circuit (WE); and 4) a circuit integrated with NFRC. Extruded polystyrene (XPS) foam boxes were placed under the samples to provide thermal insulation from the bottom surface of the acrylic chamber. To create a harsh environment with high air temperature and reduce convective heat exchange, a convection shield was employed, which consisted of a low-density polyethylene (LDPE) film that covered the measurement setup (Figure 3b). For comparison of covering the battery part, we measured the samples with and without battery cover, respectively. Figure 3c shows a thermal image of the test samples without the battery cover captured by an infrared (IR) camera (E8, FLIR) in the experimental setup. Since all samples under different covering layers have similar thermal emissivity, the IR image's color represents the samples' surface temperature. In this regard, NFRC exhibits significantly lower temperatures than the other samples except for the battery part (Figure 3c). Figure 3d shows the temperature

measurement results of the samples without the battery cover (Figure S9, Supporting Information). Under high solar power (1021 Wm^{-2}), the bare device and PDMS-integrated device exhibit significantly high temperatures (> 60 °C) that can cause skin burns in a matter of seconds. By blocking solar energy by reflection, the WE-integrated device has relatively lower temperatures than bare and PDMS-integrated devices. However, under high solar power, the temperature rises (> 45 °C) enough to cause skin damage for several hours. In the power-off state, NFRC exhibits the lowest temperature near ambient air compared to other devices. Still, in the power-on state, the device temperature rises slightly above ambient air (≈4.6 °C) due to the heating of the uncovered battery part. In the fabrication process, a thin PDMS was used as an interlayer to minimize the air gap that can cause thermal insulation between NFRC and the circuit. This strategy could help NFRC achieve stable radiative cooling over the entire area of the electronic device. Note that the combined NFRC-PDMS shows much higher cooling performance compared to the device with PDMS only. This composite performs similarly to the bare NFRC, meaning that PDMS has no effect on the cooling

**ADVANCED
SCIENCE NEWS**

www.advancedsciencenews.com

**ADVANCED
HEALTHCARE
MATERIALS**

www.advhealthmat.de

(Figure S10, Supporting Information). Figure 3e shows a thermal image of the bare device and integrated devices with battery cover captured by an IR camera in the same experimental setup. The NFRC-integrated device with a fully covered battery part shows a color indicating low temperature across the top surface area of the device to the extent that it is indistinguishable from the background color in the thermal image. Figure 3f shows the temperature measurement results of the integrated devices with the battery cover (Figure S11, Supporting Information). By covering the battery part, in the power-off state, the NFRC-integrated device exhibits the lowest temperature below ambient air, about 30 °C lower than the bare device. Even in the power-on state, it shows the lowest temperature near ambient air. Additionally, in the cooling effect evaluation, parasitic non-radiative heat gain was found to have little effect on the cooling performance in both power on/off states of the device (see Supporting Note 1 for the detailed process of the evaluation). To compare the battery performance of devices with and without NFRC, we performed the battery runtime test from a fully-charged state to discharge while wirelessly monitoring the bare device and the NFRC-integrated device in the device measurement setup (Figure 3g). Figure 3h shows the temperature data of the bare device and the NFRC-integrated device obtained by the wireless monitoring device during the battery runtime test. The NFRC-integrated device operated while logging temperature data for about 1 h and 30 min longer than the bare device, and maintained a significantly lower temperature than the bare device during the entire operating time. Moreover, in repeated battery runtime tests, the NFRC-integrated device shows constantly longer operation (10.5 and 10.8 h in indoor conditions) than the bare device (8.9 h; Figure 3i and Figure S12, Supporting Information). The power consumption shows 37.69 mW in indoor conditions, which changes to 45.63 mW under direct sunlight. On the other hand, with an applied NFRC, the power consumption maintains at 38.58 mW, showing NFRC's heat protection. The off-line discharge rate of the device is 93 μV/h, corresponding to $\approx$448 days for a complete discharge from full capacity off-line. Meanwhile, our study of device tests under various weather conditions shows no overcooling issue in cold weather scenarios (see Supporting Note 2 for the detailed estimation of cooling effect in different weather conditions).

2.4. Evaluation of Device Stability using a Radiative Cooler-Integrated Wireless System Under an Outdoor Environment

Having verified the functional robustness of the wireless circuit system integrated with thermal managing, the reliability of sensing performances of wearable biopatch was evaluated under outdoor conditions via side-to-side comparison by utilizing radiative cooling technology. We deployed a fully fabricated wearable biopatch on the user's inner wrist exposing the device's top surface to the sunlight (**Figure 4**a). The subject's arms with the wearable biopatch were placed on a table with a height of $\approx$1 m to avoid heat influence from the ground. Wireless mobile devices for real-time signal monitoring were settled 30 cm apart from the wearable devices. Two wearable devices, an NFRC-integrated device and a PDMS-integrated device, were attached to both wrists to simultaneously compare the signal

monitoring performance (Figure 4b and Movie S1, Supporting Information). The thermal image captured by the IR camera reveals that the PDMS-integrated device showed a significantly high temperature (> 45 °C) around the circuit area. In comparison, the NFRC-integrated device has a relatively low temperature ($\approx$35 °C) that is comparable to the wrist temperature (Figure 4c). After 20 min of wearing the devices, the PDMS-integrated device caused a skin burn on the wrist skin to the excessive heat of the inflamed device (Figure 4d), exhibiting the importance of thermal management in terms of user safety for long-term outdoor application in a hot environment. Figure 4e–h shows the evaluation of stable GSR recording using the biopatch when it is exposed to intense heat. First, we put the two-type of devices on the table and exposed them to the sunlight for the daytime. Raw GSR traces measured from the PDMS-integrated device showed a large baseline drift according to the temperature variation. In contrast, the signal from the NFRC-integrated device displayed a stable baseline signal (Figure 4e). A similar situation was identified when actual GSR measurement on the wrist during the sudden temperature changes by the clouds or shades (Figure 4f and Figure S13, Supporting Information). The artifacts generated by this phenomenon can be complicated to separate from actual stress arousals, affecting the analysis of stress levels. Figure 4g shows another issue of GSR signal instability by heat: an irregular data loss during measurement (Figure S14, Supporting Information). This data loss and measurement failure were also observed occasionally during the actual GSR monitoring on the wrist without the NFRC encapsulation (Figure 4h). Note that the signal instability was only observed on GSR, so we assumed that the BLE microcontroller, antenna circuits, and temperature sensor might not be the main reason for this instability. GSR circuits consist of several microchip components, including ADC, potentiometer (AD5242, Analog Devices), and op-amp (LM324N, Texas Instruments) with their operating temperatures range of −40 to 125, −40 to 105, and 0 to 70 °C, respectively. The maximum operating limit of the op-amp seems to be close to the temperature when the device was exposed to direct sunlight. The op-amp is a circuit made from multiple transistors and semiconductors so its electrical characteristics, such as gain, threshold, and resistance, can vary when the temperature changes. Irregular signal amplification of the op-amp by the excessive heat could originate the unstable GSR signal monitoring in this study. Therefore, the set of experimental data presents that thermal management of wearable devices for stable utilization outdoors, especially under extreme heat environments, is essential.

2.5. Validation of Reliable Continuous Stress Monitoring of Outdoor Workers using Soft Wearable Devices

In this section, we verified a practical performance of a fully-integrated soft wearable device for reliable stress monitoring of human subjects under outdoor working conditions (**Table 1**). We visited an agricultural area located in central Florida where environmental factors such as high temperature, humidity, and solar radiation, represent a threat to outdoor labor.[49] Subjects wore the soft biopatch on their inner wrist at the beginning of the farm works and performed work-related activities as shown in
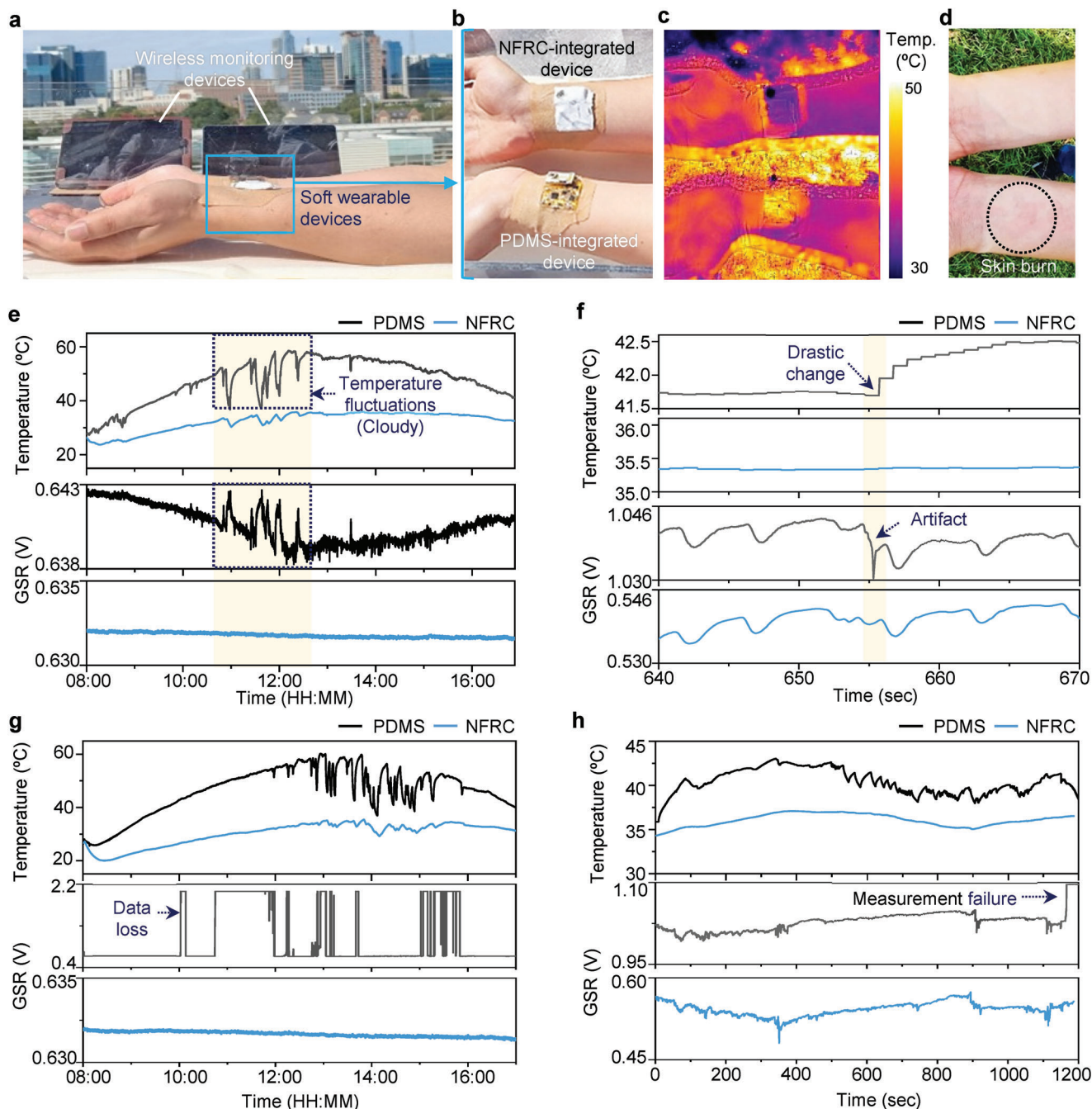
**ADVANCED
SCIENCE NEWS**

www.advancedsciencenews.com

**ADVANCED
HEALTHCARE
MATERIALS**

www.advhealthmat.de

Figure 4. Evaluation of device stability using a radiative cooler-integrated soft wireless system under an outdoor environment. a) Photograph showing experimental setup to evaluate the device stability according to heat. b) The location deploying wearable devices with the integration of PDMS or NFRC, and c) the corresponding IR image. d) Photo showing no side effects on the wrist skin using an NFRC-integrated device after 20 min of device attachment and exposure to the sunlight. A skin burn is identified under the area where the PDMS-encapsulated device is affixed. e–h) Stability comparison of GSR recording between PDMS-integrated and NFRC-integrated devices exposed to the sunlight: e) baseline drift, f) artifact generation by sudden temperature changes by shades, g) data loss, and h) measurement failure.

Figure 5a. To compare the reliability of the device, two types of devices encapsulated with NFRC and PDMS were attached on both wrists during activities (Figure 5b and Movie S2, Supporting Information). Figure 5c captures three representative activities of agricultural work (harvesting field crops, loading containers, and resting) that the subject follows while simultaneously mea-

suring GSR and temperature signals from both devices. A set of graphs in Figure 5d shows raw GSR and temperature data, measured by both devices encapsulated with NFRC and PDMS on the wrist from the entire measurement time, including the three activities of harvesting, loading, and resting (Figure S15, Supporting Information). As expected, temperature data measured by the

**ADVANCED
SCIENCE NEWS**

www.advancedsciencenews.com

**ADVANCED
HEALTHCARE
MATERIALS**

www.advhealthmat.de

Table 1. Comparison of recent studies on wearable stress monitoring devices.

Ref. (published date)	Device form factor	Outdoor field validation	High temperature demonstration	Thermal management with cooling layers	Operation temperature	Cooling performance	Application	Used sensors	Power consumption, GSR sampling, GSR resolution
This work	Soft patch-type sensor	Yes	Yes	Yes	35–45 °C	30 °C lower than a bare device (5 °C below ambient air)	Outdoor worker	GSR, temperature	37.69 mW with cooling, 45.63 mW without cooling, 5 Hz, 3 µV
[19] (8/28/2022)	Rigid watch-type sensor	No	No	Yes	24–29 °C	–	Urban pedestrian	GSR, PPG	46.25 mW, 4 Hz, 1 nS
[21] (7/7/2021)	Rigid watch-type sensor	No	No	No	29–31 °C	–	Construction worker	GSR, temperature, PPG	46.25 mW, 4 Hz, 1 nS
[51] (3/25/2019)	Rigid watch-type sensor	No	No	Yes	Not mentioned	–	Urban pedestrian	GSR, heart rate	46.25 mW, 4 Hz, 1 nS
[52] (1/6/2021)	Rigid box and wired ear modules	No	No	Yes	Not mentioned	–	Vehicle driver	Heart rate, temperature, accelerometer	Not mentioned
[20] (6/17/2022)	Rigid module-integrated T-shirt	No	No	No	Not mentioned	–	Indoor researcher	ECG	10.79 mW – –
[22] (11/4/2020)	Stretchable patch-type sensor	No	No	No	Not mentioned	–	Household worker	GSR, temperature	58.14 mW, 1–5 Hz –

PDMS-integrated device shows larger signal fluctuation than the NFRC device due to strong sunlight exposure during the work tasks. In addition, unstable recording of GSR was identified on the PDMS-integrated device due to the motion artifacts originating from the excessive sweat under the heated device weakening the adhesion of biopatch on the skin. Stable GSR data from the device covered with the NFRC was recorded during the entire monitoring time, indicating reliable device adhesion to the skin. Recorded data were analyzed through the multi-step processes described in Figure S16, Supporting Information, including phasic element extraction and peak identification.[22,50] The raw GSR signals and collected phasic elements in the specific time window according to the three activities are shown in Figure 5e,f, respectively. Note that a huge root-mean-square (RMS) value (2.80) from the PDMS-covered device during the loading task was calculated due to the motion artifacts compared to the similar work-related task, harvesting (0.47) while the NFRC device showed relatively similar RMS values between the two tasks (1.31 and 1.14). The average numbers of phasic peaks counted within 60-s intervals according to the different tasks were summarized in Figure 5g. The NFRC-integrated device shows a significant reduction in peak numbers during resting (3.33) compared to the other work-related tasks (10.67 and 13.33), validating both work-related tasks cause more stress to the subject while the stationary resting activity reduces the stress. On the other hand, the PDMS-integrated device showed a large deviation of the peak numbers between harvesting (0.67) and loading (11.33) tasks, describing the capability of analysis failure using the device without heat manage-

ment under outdoor conditions. Figure 5h represents the summarized data of counted peaks measured by the NFRC-integrated device for the entire work time, visualized by the relative intensity of stress level. The high-stress levels (red area) are shown during the work-related tasks, whereas the stress level was generally relieved when the subject rested. The comparison study with a commercial physiological monitor (BioRadio, Great Lakes NeuroTechnologies) confirms that our device captures a similar level of stress intensity (Figure S17, Supporting Information). The result with different intervals (30 and 10 s) for peak counts also showed a similar trend of stress migration (Figure S18, Supporting Information). Collectively, the wearable device with an effective heat management technique allows successful and reliable continuous stress monitoring and quantification of outdoor laborers' working stress under severe heat conditions (Table S1, Supporting Information).

3. Conclusion

This paper reports an NFRC-integrated wireless soft wearable bioelectronics for thermal management and reliable continuous monitoring and quantifying outdoor workers' stress in hot environments. This wearable system demonstrates robust device operation even under high-temperature environments caused by extreme sunlight, showing promise as an effective wearable health monitor for various outdoor applications. Validation of the wearable device's functional robustness and enhanced performance with stable sensing performances by utilizing a cooling
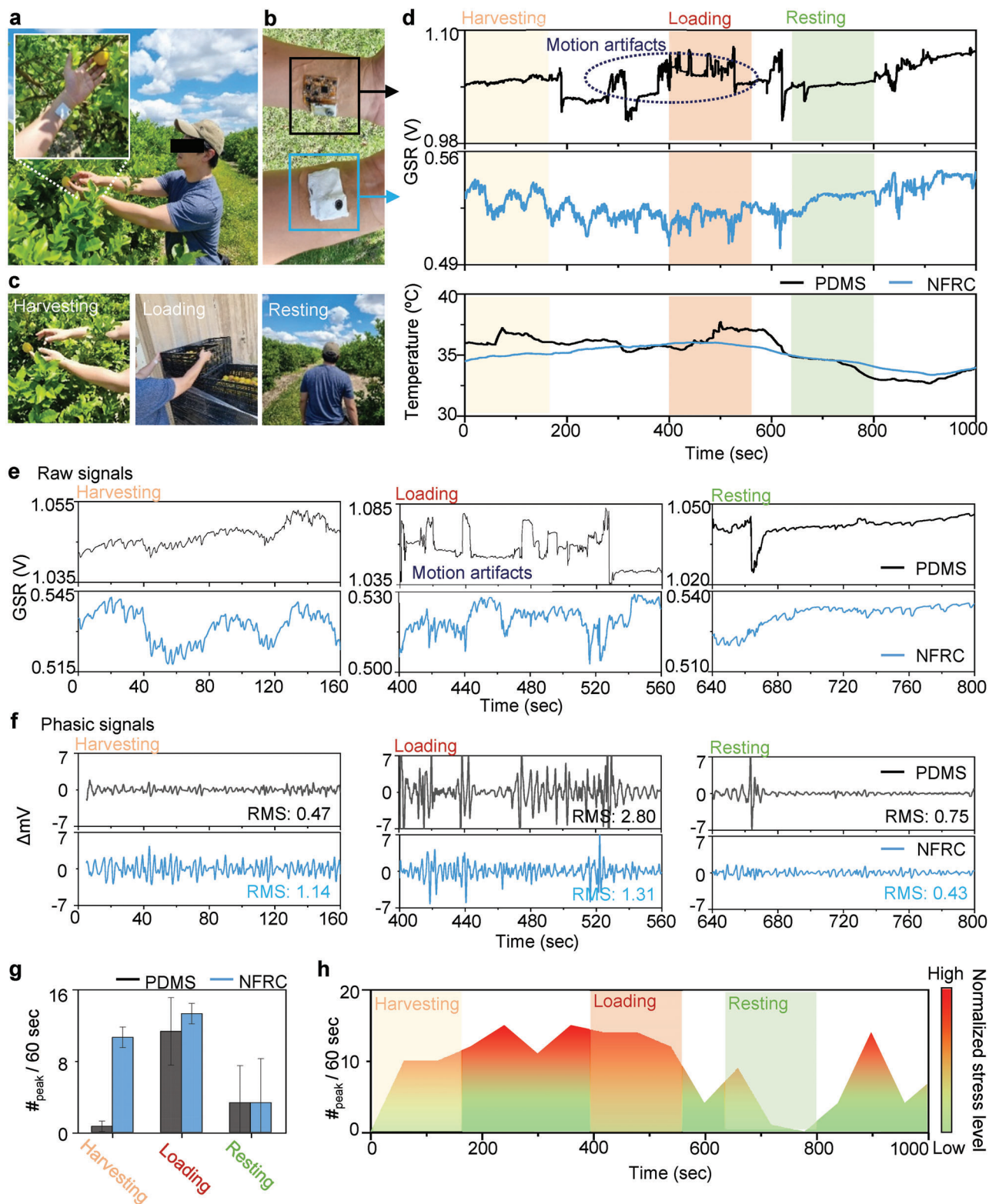
**ADVANCED
SCIENCE NEWS**

www.advancedsciencenews.com

**ADVANCED
HEALTHCARE
MATERIALS**

www.advhealthmat.de

Figure 5. Verification of reliable stress monitoring of outdoor workers using soft wearable devices with radiative cooler. a) Photos capturing a soft wearable device attached to the subject's wrist during outdoor agricultural work-related activities. b) Photos showing two types of devices encapsulated with NFRC and PDMS mounted on both wrists. c) Continuous stress monitoring with different activities, including harvesting field crops, loading containers, and resting. d) Raw GSR and temperature data measured on the wrist by both devices with NFRC and PDMS during working activities outside. e) Raw GSR signals and f) their phasic elements at the specific time window according to the three work activities. g) The average peak counts for three activities (n = 3). h) Visualized relative intensity of stress level measured by NFRC-encapsulated device during work.

**ADVANCED
SCIENCE NEWS**

www.advancedsciencenews.com

**ADVANCED
HEALTHCARE
MATERIALS**

www.advhealthmat.de

layer captures that adequate thermal controls under scorching environments are essential. Furthermore, demonstrating continuous, real-time, portable stress monitoring and analysis using an NFRC-integrated device with actual agricultural activities has shown the device's performance in real-life working environments.

4. Experimental Section

Fabrication of Nanomembrane Electrodes: PDMS (Sylgard 184, Dow Corning) was spin-coated on a glass slide. 12.7 µm thick polyimide (PI) sheet (50HN Kapton Film, DuPont) was laminated onto the PDMS-coated glass slide. Then, 5/200 nm thick Cr/Au layers were deposited by an e-beam evaporator (Denton Explorer). The PI/Cr/Au layers were serpentine-patterned by a femtosecond IR laser micromachining tool (WS-Flex, Optec) for two cycles with 50 W of laser power. A water-soluble tape (ASWT-2, AQUASOL) was used to transfer the functional pieces from the PDMS/glass substrate to a fabric substrate (9907T, 3M) coated with a silicone adhesive (Silbione, Elkem). Finally, a low-modulus elastomer (Ecoflex 30, Smooth-On) was applied along the interconnect lines for insulation.

Fabrication of an Integrated Wireless Electronic System: Microchip components were soldered onto a flexible circuit board using reflow soldering paste (SMDLTLFP10T5, Chip Quik) at 200 °C. A rechargeable lithium-ion polymer battery (110 mAh, Adafruit) integrated with a slide switch and a magnetic charging port was linked to the circuit, and a PDMS layer that mixed with a white coloring pigment (Silc Pig, Smooth-On) was coated over the circuit, cured in a vacuum oven at 50 °C for 0.5 h. The circuit and substrate were bonded with the PDMS and connected by a flexible conductive film (HST-9805-210, Elform). Finally, the connection was encapsulated with the PDMS again. A schematic illustration of the fabrication process flow for wearable biopatch assembly can be found in Figure S19, Supporting Information.

Fabrication of NFRC Films: PVDF-HFP solution (20 wt %) was prepared by dissolving PVDF-HFP pellets in a Dimethylformamide (DMF)–acetone mixture (1/1, w/w) and agitating the mixture in a water bath at 70 °C to obtain a uniform and transparent solution. Then, the PVDF-HFP solution was put into a syringe installed on an electrospinning device with the electrospinning operating parameters of injection speed 2 mL h^{-1}, needle-to-collecting device distance 15 cm, and voltage 20 kV. The thickness of the electrospun PVDF-HFP nanofiber could be adjusted by controlling the spinning time. After electrospinning, the PVDF-HFP film was annealed at 135 °C for 5 min on a hot plate by applying pressure on both sides with two slide glasses. A schematic illustration of the fabrication process flow for NFRC film can be found in Figure S20, Supporting Information.

Structural and Spectral Analysis: To determine the optical reflectance of WE and NFRC in the range of 280 to 2500 nm, a UV–vis–NIR spectrophotometer (Lambda 950, Perkin Elmer, Inc.) with an integrating sphere was utilized. The emissivity spectra were derived using a Fourier transform infrared spectrometer (VERTEX 70v, Bruker) equipped with an Au-coated integrating sphere, where emissivity (E), reflectivity (R), and transmittance (T) are related by the equation $E = 1 - R + T$. Structural analyses were conducted using SEM (S-4700, Hitachi Hi-Tech).

Thermal Characterization of Integrated Wearable Devices: To ensure dependable thermal characterization for investigating the cooling capabilities of the devices, an XPS foam was prepared to provide thermal insulation between the transformative devices and the bottom surface of the acrylic chamber. The double-sided thermal conductive tape was applied onto the thermal insulation blocks, and adhesive temperature sensors (ST-50, RKC Instrument Inc.) were attached to both the top and bottom sides of the samples. An ambient air sensor was placed within an Al-coated paper box to record the temperature of the naturally convective air in the chamber, and to prevent it from overheating due to solar irradiance. Finally, the entire acrylic chamber was covered with an LDPE film to minimize the convection effect, and a pyranometer (CMP6, Kipp & Zonen) was positioned next to the acrylic chamber to measure solar irradiance.

Data Analysis: The phasic components of GSR were extracted from raw data by using the Fast Fourier transform (FFT) with a band-pass filter, 0.2–1 Hz. The RMS value of the phasic signal was calculated as a threshold level to detect signal peaks. The peaks shown over the threshold level were defined as an arousal status of stress, counted the number of peaks within a certain time interval.

Human Subject Study: This pilot study involved healthy subjects and was conducted by following the Georgia Tech-approved IRB protocol (#H23035). Prior to the study, all subjects agreed with the study procedures and provided signed consent forms.

Supporting Information

Supporting Information is available from the Wiley Online Library or from the author.

Conflict of Interest

Georgia Tech has a pending US patent application.

Author Contributions

H.K. and Y.J.Y. contributed equally to this work. H.K., Y.M.S., and W.-H.Y. designed the research conceptualization. H.K., Y.J.Y. performed formal analysis., H.K., Y.J.Y., J.H.Y., and S.-Y.H. fabricated the sensor and analyzed the data. H.K., Y.J.Y., Y.M.S., and W.-H.Y. wrote the paper.

Data Availability Statement

The data that support the findings of this study are available on request from the corresponding author. The data are not publicly available due to privacy or ethical restrictions.

**ADVANCED
SCIENCE NEWS**

www.advancedsciencenews.com

**ADVANCED
HEALTHCARE
MATERIALS**

www.advhealthmat.de

[1] B. L. Jacklitsch, W. J. Williams, K. Musolin, A. Coca, J.-H. Kim, N. Turner, *NIOSH Criteria for a Recommended Standard: Occupational Exposure to Heat and Hot Environments* 2016.

[2] D. M. Gubernot, G. B. Anderson, K. L. Hunting, *Int. J. Biometeorol.* 2014, 58, 1779.

[3] J. D. Runkle, C. Cui, C. Fuhrmann, S. Stevens, J. Del Pinal, M. M. Sugg, *Environ. Int.* 2019, 129, 229.

[4] J. Goh, J. Pfeffer, S. A. Zenios, *Manage. Sci.* 2016, 62, 608.

[5] J. Hansen, M. Sato, R. Ruedy, *Proc. Natl. Acad. Sci. USA* 2012, 109, E2415.

[6] B. Jones, B. C. O'Neill, L. McDaniel, S. McGinnis, L. O. Mearns, C. Tebaldi, *Nat. Clim. Change* 2015, 5, 652.

[7] E. Heber, D. Lehr, D. D. Ebert, M. Berking, H. Riper, *J. Med. Internet Res.* 2016, 18, 21.

[8] Y. S. Can, B. Arnrich, C. Ersoy, *J. Biomed. Inf.* 2019, 92, 103139.

[9] T. Âkerstedt, *Scand. J. Work, Environ. Health* 2006, 32, 493.

[10] A. D. Flouris, P. C. Dinas, L. G. Ioannou, L. Nybo, G. Havenith, G. P. Kenny, T. Kjellstrom, *Lancet Planet. Health* 2018, 2, 521.

[11] O. Dehzangi, V. Rajendra, M. Taherisadr, *Sensors* 2018, 18, 503.

[12] J.-J. Cabibihan, S. S. Chauhan, *IEEE Trans. Affective Comput.* 2015, 8, 108.

[13] W. Boucsein, *Electrodermal Activity*, Springer, New York 2012.

[14] M. Benedek, C. Kaernbach, *J. Neurosci. Methods* 2010, 190, 80.

[15] R. Subramanian, J. Wache, M. K. Abadi, R. L. Vieriu, S. Winkler, N. Sebe, *IEEE Trans. Affective Comput.* 2016, 9, 147.

[16] C. Kappeler-Setz, F. Gravenhorst, J. Schumm, B. Arnrich, G. Tröster, *Pers. Ubiquitous Comput.* 2013, 17, 261.

[17] H. Kim, Y. S. Kim, M. Mahmood, S. Kwon, N. Zavanelli, H. S. Kim, Y. S. Rim, F. Epps, W. H. Yeo, *Adv. Sci.* 2020, 7, 2000810.

[18] A. S. Svetlov, M. M. Nelson, P. D. Antonenko, J. P. McNamara, R. Bussing, *Heliyon* 2019, 5, 01351.

[19] A. Torku, A. P. Chan, E. H. Yung, J. Seo, *Build. Environ.* 2022, 224, 109533.

[20] M. B. Bin Heyat, F. Akhtar, S. J. Abbas, M. Al-Sarem, A. Alqarafi, A. Stalin, R. Abbasi, A. Y. Muaad, D. Lai, K. Wu, *Biosensors* 2022, 12, 427.

[21] S. Shakerian, M. Habibnezhad, A. Ojha, G. Lee, Y. Liu, H. Jebelli, S. Lee, *Saf. Sci.* 2021, 142, 105395.

[22] H. Kim, Y.-S. Kim, M. Mahmood, S. Kwon, F. Epps, Y. S. Rim, W.-H. Yeo, *Biosens. Bioelectron.* 2021, 173, 112764.

[23] J. Mandal, Y. Fu, A. C. Overvig, M. Jia, K. Sun, N. N. Shi, H. Zhou, X. Xiao, N. Yu, Y. Yang, *Science* 2018, 362, 315.

[24] Y. Zhai, Y. Ma, S. N. David, D. Zhao, R. Lou, G. Tan, R. Yang, X. Yin, *Science* 2017, 355, 1062.

[25] S. Zeng, S. Pian, M. Su, Z. Wang, M. Wu, X. Liu, M. Chen, Y. Xiang, J. Wu, M. Zhang, *Science* 2021, 373, 692.

[26] P.-C. Hsu, A. Y. Song, P. B. Catrysse, C. Liu, Y. Peng, J. Xie, S. Fan, Y. Cui, *Science* 2016, 353, 1019.

[27] L. Cai, Y. Peng, J. Xu, C. Zhou, C. Zhou, P. Wu, D. Lin, S. Fan, Y. Cui, *Joule* 2019, 3, 1478.

[28] Y. Peng, J. Chen, A. Y. Song, P. B. Catrysse, P.-C. Hsu, L. Cai, B. Liu, Y. Zhu, G. Zhou, D. S. Wu, *Nat. Sustainability* 2018, 1, 105.

[29] M. Alberghini, S. Hong, L. M. Lozano, V. Korolovych, Y. Huang, F. Signorato, S. H. Zandavi, C. Fucetola, I. Uluturk, M. Y. Tolstorukov, *Nat. Sustain.* 2021, 4, 715.

[30] X. Yin, R. Yang, G. Tan, S. Fan, *Science* 2020, 370, 786.

[31] S.-Y. Heo, G. J. Lee, D. H. Kim, Y. J. Kim, S. Ishii, M. S. Kim, T. J. Seok, B. J. Lee, H. Lee, Y. M. Song, *Sci. Adv.* 2020, 6, abb1906.

[32] K. Tang, K. Dong, J. Li, M. P. Gordon, F. G. Reichertz, H. Kim, Y. Rho, Q. Wang, C.-Y. Lin, C. P. Grigoropoulos, *Science* 2021, 374, 1504.

[33] S. Wang, T. Jiang, Y. Meng, R. Yang, G. Tan, Y. Long, *Science* 2021, 374, 1501.

[34] S. Y. Heo, D. H. Kim, Y. M. Song, G. J. Lee, *Adv. Energy Mater.* 2022, 12, 2103258.

[35] G. J. Lee, S.-Y. Heo, S. Son, K. M. Kang, H. Lee, Y. M. Song, *Opt. Express* 2021, 29, 31364.

[36] G. J. Lee, D. H. Kim, S.-Y. Heo, Y. M. Song, *ACS Appl. Mater. Interfaces* 2020, 12, 53206.

[37] J. Song, W. Zhang, Z. Sun, M. Pan, F. Tian, X. Li, M. Ye, X. Deng, *Nat. Commun.* 2022, 13, 4805.

[38] X. Huang, J. Mandal, J. Xu, A. P. Raman, *Joule* 2022, 6, 2762.

[39] J. Li, X. Wang, D. Liang, N. Xu, B. Zhu, W. Li, P. Yao, Y. Jiang, X. Min, Z. Huang, *Sci. Adv.* 2022, 8, abq0411.

[40] Q. Zhang, Y. Wang, Y. Lv, S. Yu, R. Ma, *Proc. Natl. Acad. Sci. USA* 2022, 119, 2207353119.

[41] Y. Xu, B. Sun, Y. Ling, Q. Fei, Z. Chen, X. Li, P. Guo, N. Jeon, S. Goswami, Y. Liao, *Proc. Natl. Acad. Sci. USA* 2020, 117, 205.

[42] M. H. Kang, G. J. Lee, J. H. Lee, M. S. Kim, Z. Yan, J. W. Jeong, K. I. Jang, Y. M. Song, *Adv. Sci.* 2021, 8, 2004885.

[43] S. H. Byun, J. H. Yun, S. Y. Heo, C. Shi, G. J. Lee, K. C. Agno, K. I. Jang, J. Xiao, Y. M. Song, J. W. Jeong, *Adv. Sci.* 2022, 9, 2202549.

[44] Y. S. Kim, J. Kim, R. Chicas, N. Xiuhtecutli, J. Matthews, N. Zavanelli, S. Kwon, S. H. Lee, V. S. Hertzberg, W. H. Yeo, *Adv. Healthcare Mater.* 2022, 11, 2200170.

[45] Y.-T. Kwon, J. J. Norton, A. Cutrone, H.-R. Lim, S. Kwon, J. J. Choi, H. S. Kim, Y. C. Jang, J. R. Wolpaw, W.-H. Yeo, *Biosens. Bioelectron.* 2020, 165, 112404.

[46] W. Jing, S. Zhang, W. Zhang, Z. Chen, C. Zhang, D. Wu, Y. Gao, H. Zhu, *ACS Appl. Mater. Interfaces* 2021, 13, 29558.

[47] D. Li, X. Liu, W. Li, Z. Lin, B. Zhu, Z. Li, J. Li, B. Li, S. Fan, J. Xie, *Nat. Nanotechnol.* 2021, 16, 153.

[48] J. Li, Y. Liang, W. Li, N. Xu, B. Zhu, Z. Wu, X. Wang, S. Fan, M. Wang, J. Zhu, *Sci. Adv.* 2022, 8, abj9756.

[49] J. Flocks, V. Vi Thien Mac, J. Runkle, J. A. Tovar-Aguilar, J. Economos, L. A. McCauley, *J. Agromedicine* 2013, 18, 350.

[50] F. Hernando-Gallego, D. Luengo, A. Artés-Rodríguez, *IEEE J. Biomed. Health Inf.* 2017, 22, 1385.

[51] A. Birenboim, M. Dijst, F. E. Scheepers, M. P. Poelman, M. Helbich, *Prof. Geogr.* 2019, 71, 449.

[52] N. Ahmed, R. J. Rony, *Qual. User Exper.* 2021, 6, 4.